Supplementary Information

Photoactivation of the Orange Carotenoid Protein Requires Two Light-Driven Reactions Mediated by a Metastable Monomeric Intermediate

Justin B. Rose,[a] José A. Gascón,[b] Markus Sutter,[c,d,e] Damien I. Sheppard,[c] Cheryl A. Kerfeld,[c,d,e] and Warren F. Beck[a,*]

a. Department of Chemistry, Michigan State University, East Lansing, Michigan 48824-1322 USA

b. Department of Chemistry, University of Connecticut, Storrs, Connecticut 06269-3060 USA

c. MSU–DOE Plant Research Laboratory, Michigan State University, East Lansing, Michigan 48824-1322 USA

d. Environmental Genomics and Systems Biology Division, Lawrence Berkeley National Laboratory, Berkeley, California 94720, USA

e. Molecular Biophysics and Integrated Bioimaging Division, Lawrence Berkeley National Laboratory, Berkeley, California 94720, USA

*Corresponding author. Email: beckw@msu.edu

Table of Contents

Figure S1. Photoactivation and dark recovery of OCP at 273 K in the presence of 60% (v/v) glycerol. 4

Figure S2. Singular-value decomposition analysis of the time evolution of the absorption spectrum of OCP at 273 K in the presence of 60% (v/v) glycerol during continuous 430-nm illumination (275 μW). 4

Figure S3. Global modeling of the time evolution of the absorption spectrum of OCP at 273 K in the presence of 60% (v/v) glycerol under continuous 430-nm illumination (220 μW), applying a two-compartment kinetic model: $OCP^O \xrightarrow{1/\tau} OCP^R$. 5

Figure S4. Singular-value decomposition analysis of the time evolution of the absorption spectrum of OCP at 293 K in the presence of 60% (v/v) glycerol in the dark following continuous 430-nm illumination (275 μW). 6

Figure S5. Global modeling of the time evolution of the absorption spectrum of OCP at 293 K in the presence of 60% (v/v) glycerol in the dark following continuous 430-nm illumination (275 μW), applying a two-compartment kinetic model: $OCP^R \xrightarrow{1/\tau} OCP^O$. 6

Figure S6. Global modeling of the time evolution of the absorption spectrum of OCP at 293 K in the presence of 60% (v/v) glycerol in the dark following continuous 430-nm illumination (275 μW), applying a three-compartment kinetic model: $OCP^R \xrightarrow{1/\tau_{-2}} OCP^{I'} \xrightarrow{1/\tau_{-1}} OCP^O$. 7

Figure S7. Singular-value decomposition analysis of the time evolution of the absorption spectrum of OCP at 293 K in the absence of glycerol during continuous 430-nm illumination (275 μW). 8

Figure S8. Global modeling of the time evolution of the absorption spectrum of OCP at 293 K in the absence of glycerol under continuous 430-nm illumination (545 μW), applying a two-compartment kinetic model: $OCP^O \xrightarrow{1/\tau} OCP^R$. 9

Figure S9. Singular-value decomposition analysis of the time evolution of the absorption spectrum of OCP at 293 K in the absence of glycerol in the dark following continuous 430-nm illumination (545 μW). 10

Figure S10. Global modeling of the time evolution of the absorption spectrum of OCP at 293 K in the absence of glycerol in the dark following continuous 430-nm illumination (545 μW), applying a two-compartment kinetic model: $OCP^R \xrightarrow{1/\tau} OCP^O$. 10

Figure S11. Global modeling of the time evolution of the absorption spectrum of OCP at 293 K in the absence of glycerol in the dark following continuous 430-nm illumination (545 μW), applying a three-compartment kinetic model: $OCP^R \xrightarrow{1/\tau_{-2}} OCP^{I'} \xrightarrow{1/\tau_{-1}} OCP^O$. 11

Figure S12. Comparison of the evolution-associated spectra obtained from the global models for the forward photoactivation at 273 K (Fig. 3) and reverse recovery at 293 K (Figs. 5 and S6) of OCP in the presence of 60% (v/v) glycerol. 12

Figure S13. Singular-value decomposition analysis of the time evolution of the absorption spectrum of OCP at 293 K in the presence of 60% (v/v) glycerol during continuous 430-nm illumination (556 μW). 13

Figure S14. Global modeling of the time evolution of the absorption spectrum of OCP at 293 K in the presence of 60% (v/v) glycerol under continuous 430-nm illumination (556 μW), applying a two-compartment kinetic model: $OCP^O \xrightarrow{1/\tau} OCP^R$. 13

Figure S15. Global modeling of the time evolution of the absorption spectrum of OCP at 293 K in the presence of 60% (v/v) glycerol under continuous 430-nm illumination (556 μW), applying a three-compartment kinetic model: $OCP^O \xrightarrow{1/\tau_1} OCP^I \xrightarrow{1/\tau_2} OCP^R$. 14

Figure S16. Global modeling of the time evolution of the absorption spectrum of OCP at 293 K in the dark in the absence of glycerol following continuous 430-nm illumination (700 μW), applying a three-compartment kinetic model: $OCP^R \xrightarrow{1/\tau_{-2}} OCP^{I'} \xrightarrow{1/\tau_{-1}} OCP^O$. The absorption at 500 nm of the dark adapted OCP^R solution present prior to illumination was 0.06. 15

Figure S17. Global modeling of the time evolution of the absorption spectrum of OCP at 293 K in the dark in the absence of glycerol following continuous 430-nm illumination (700 μW), applying a three-compartment kinetic model: $OCP^R \xrightarrow{1/\tau_{-2}} OCP^{I'} \xrightarrow{1/\tau_{-1}} OCP^O$. The absorption at 500 nm of the dark adapted OCP^R solution present prior to illumination was 0.6. 16

Table S1. Multimode Brownian oscillator (MBO) model parameters[a,b] for the simulated absorption spectra shown in Fig. 7 for canthaxanthin (CAN) in 2-methyltetrahydrofuran and in the photoactivation of OCP at 293 K in the absence of glycerol. 17

Analysis of the Kinetics of the Dark Recovery Response 17

Computational Methods 19

References 20

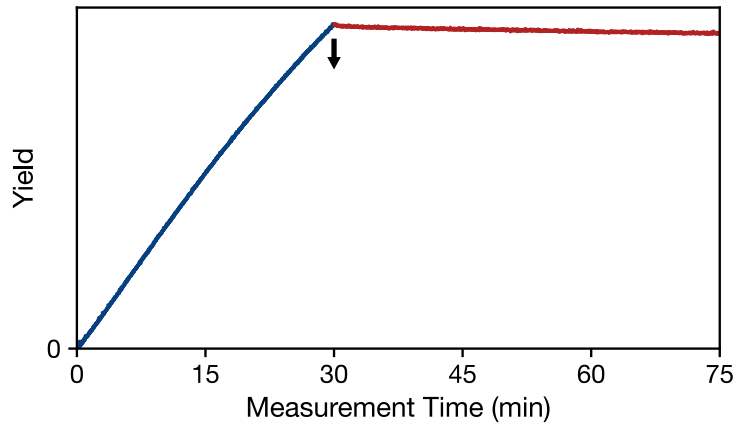

Figure S1. Photoactivation and dark recovery of the Orange Carotenoid Protein (OCP) at 273 K in the presence of 60% (v/v) glycerol. The sample was illuminated at 430 nm (275 µW) for 30 minutes (blue) followed by incubation in the dark starting at the down arrow (red). The relative yield was determined as in Fig. 2 using the the integral of the absolute value of the light – initial dark difference spectrum as a function of time.

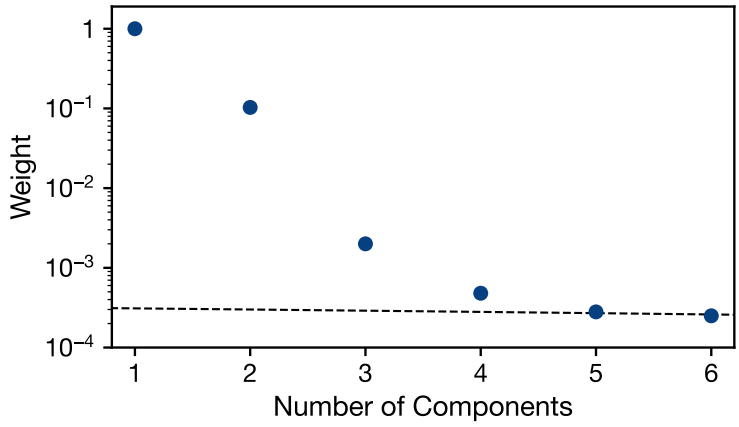

Figure S2. Singular-value decomposition (SVD) analysis of the time evolution of the absorption spectrum of OCP at 273 K in the presence of 60% (v/v) glycerol during continuous 430-nm illumination (275 µW). The dashed line marks the noise level of the data set.

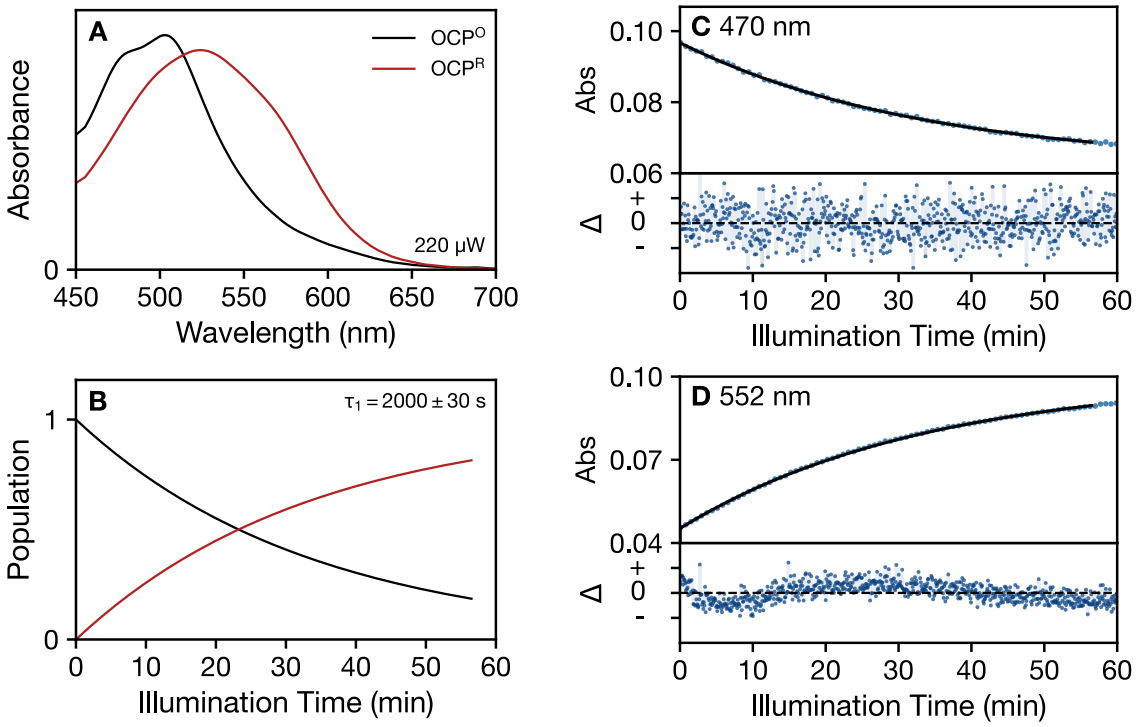

Figure S3. Global modeling of the time evolution of the absorption spectrum of OCP at 273 K in the presence of 60% (v/v) glycerol under continuous 430-nm illumination (220 µW), applying a two-compartment kinetic model: $OCP^O \xrightarrow{1/\tau} OCP^R$. (a) Evolution-associated absorption spectra for the two kinetic compartments: dark-adapted OCP^O reactant (black) and the final OCP^R product (red). (b) Time evolution of the populations for the OCP^O and OCP^R kinetic compartments. (c, d) Fit of the global model (black) to the observed absorption (blue dots) at two detection wavelengths, 470 nm and 552 nm, as marked in Fig. 2a and b, showing the single-wavelength absorption transients (top panel) and residuals (bottom panel). The residuals (Δ = data – global model) are shown with a 20× zoom factor for the absorbance ordinate.

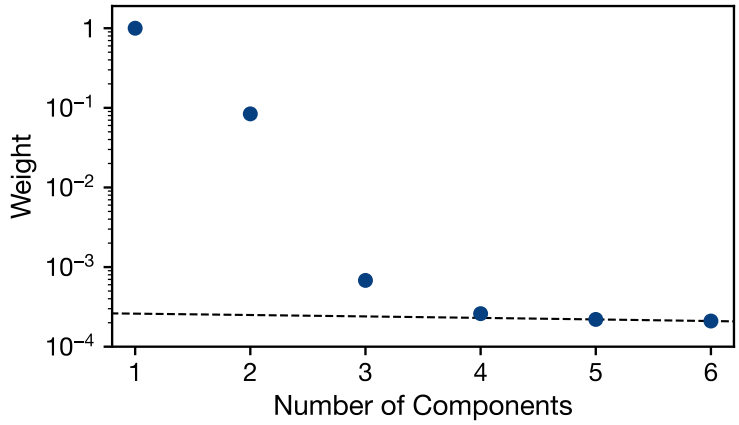

Figure S4. Singular-value decomposition (SVD) analysis of the time evolution of the absorption spectrum of OCP at 293 K in the presence of 60% (v/v) glycerol in the dark following continuous 430-nm illumination (275 µW). The dashed line marks the noise level of the data set.

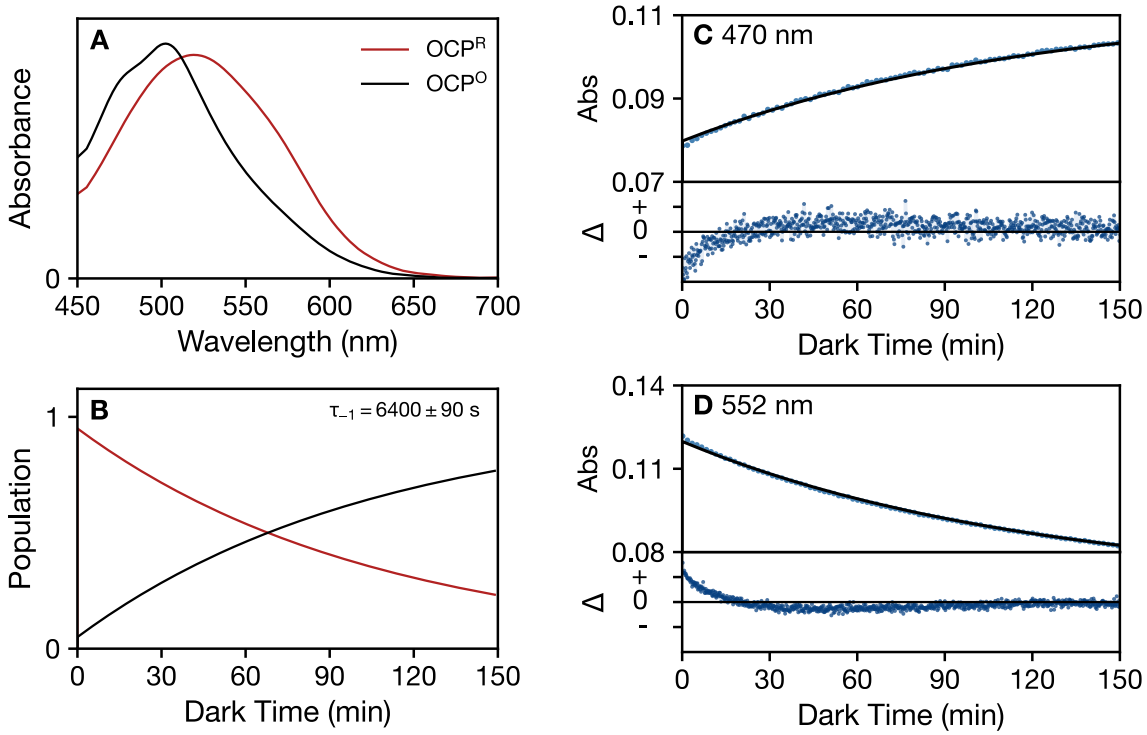

Figure S5. Global modeling of the time evolution of the absorption spectrum of OCP at 293 K in the presence of 60% (v/v) glycerol in the dark following continuous 430-nm illumination (275 µW), applying a two-compartment kinetic model: $OCP^R \xrightarrow{1/\tau} OCP^O$. (a) Evolution-associated absorption spectra for the two kinetic compartments: OCP^R

reactant (red) and the OCP^O product (black). (b) Time evolution of the populations for the OCP^R and OCP^O kinetic compartments; the initial mixture of $OCP^R(0) = 0.95$ and $OCP^O(0) = 0.05$ was determined from modeling of the prior photoactivation response. (c, d) Fit of the global model (black) to the observed absorption (blue dots) at two detection wavelengths, 470 nm and 552 nm, showing the single-wavelength absorption transients (top panel) and residuals (bottom panel). The residuals (Δ = data – global model fit) are shown with a 10× zoom factor for the absorbance ordinate.

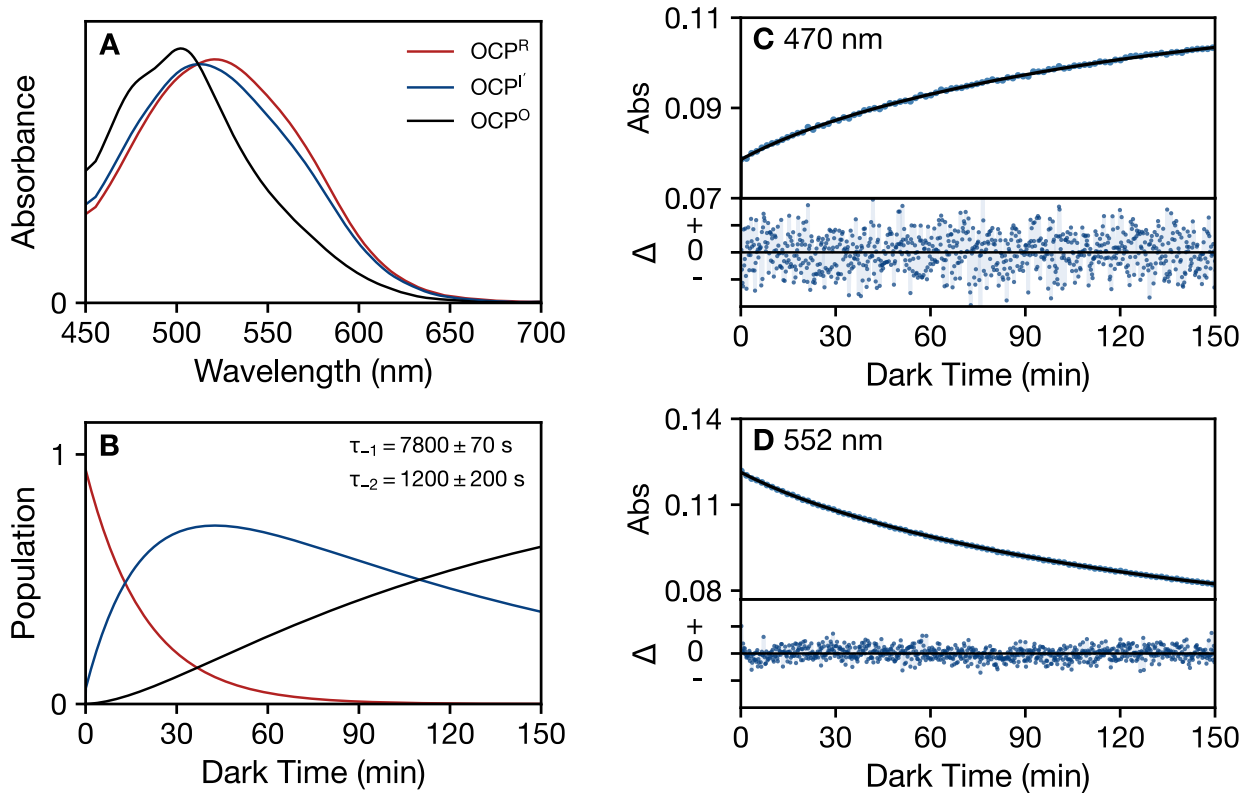

Figure S6. Global modeling of the time evolution of the absorption spectrum of OCP at 293 K in the dark in the presence of 60% (*v*/*v*) glycerol following continuous 430-nm illumination (275 μW), applying a three-compartment kinetic model: $OCP^R \xrightarrow{1/\tau_{-2}} OCP^{I'} \xrightarrow{1/\tau_{-1}} OCP^O$. Panels (a) and (b) are shown in Fig. 5 (c) and (d), respectively. (a) Evolution-associated absorption spectra for the three kinetic compartments: OCP^R reactant (red), the $OCP^{I'}$ intermediate (blue), and the final OCP^O product (black). (b) Time evolution of the populations for the OCP^R, $OCP^{I'}$, and OCP^O kinetic compartments; the initial mixture of $OCP^R(0) = 0.94$, $OCP^I(0) = 0.06$, and $OCP^O(0) = 0.00$ was determined from modeling of the prior photoactivation response. (c, d) Fit of the global model (black) to the observed

absorption (blue dots) at two detection wavelengths, 470 nm and 552 nm, showing the single-wavelength absorption transients (top panel) and residuals (bottom panel). The residuals (Δ = data – global model fit) are shown with a 20× zoom factor for the absorbance ordinate.

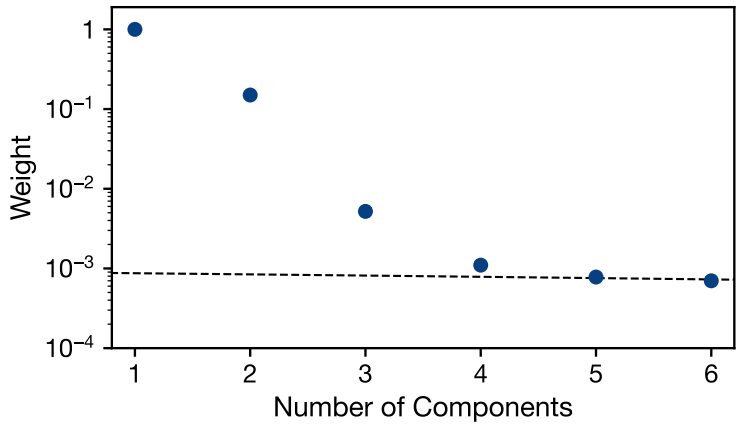

Figure S7. Singular-value decomposition analysis of the time evolution of the absorption spectrum of OCP at 293 K in the absence of glycerol during continuous 430-nm illumination (275 μW). The dashed line marks the noise level of the data set.

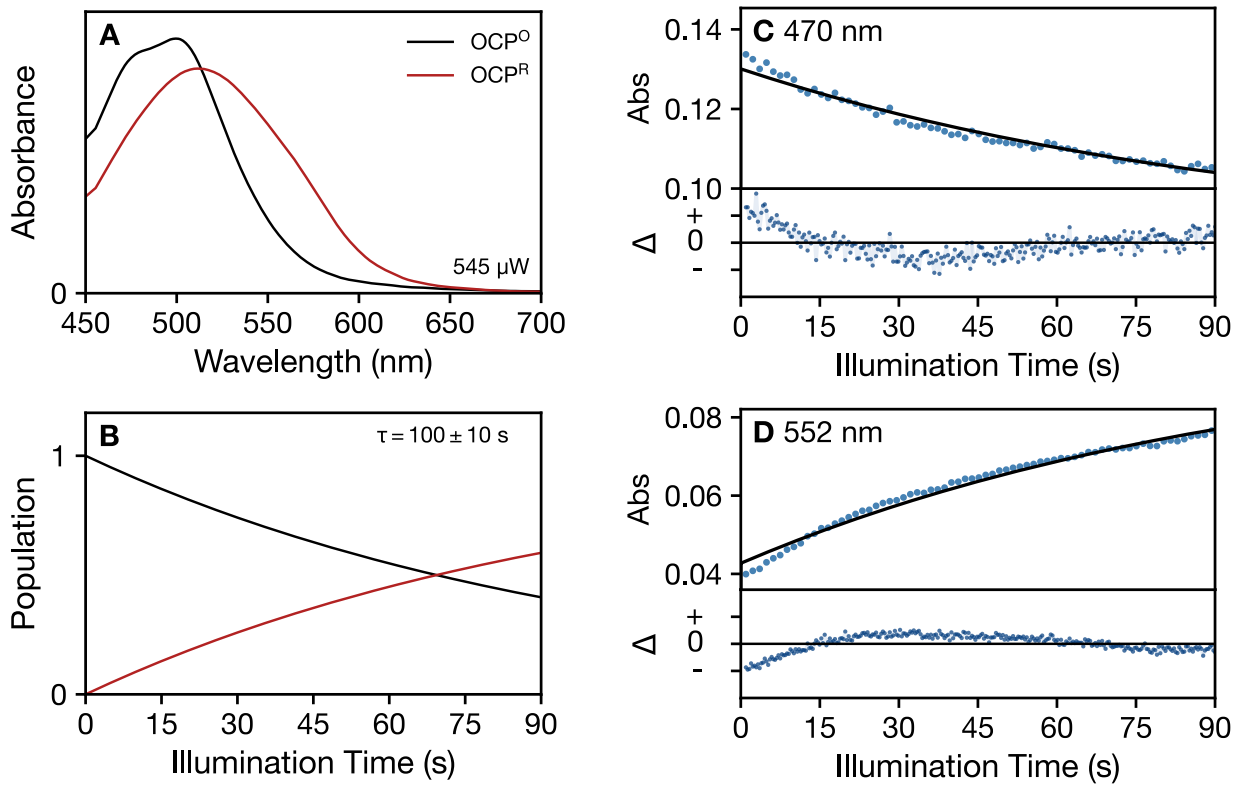

Figure S8. Global modeling of the time evolution of the absorption spectrum of OCP at 293 K in the absence of glycerol under continuous 430-nm illumination (545 µW), applying a two-compartment kinetic model: $OCP^O \xrightarrow{1/\tau} OCP^R$. (a) Evolution-associated absorption spectra for the two kinetic compartments: dark-adapted OCP^O reactant (black) and the final OCP^R product (red). (b) Time evolution of the populations for the OCP^O and OCP^R kinetic compartments. (c, d) Fit of the global model (black) to the observed absorption (blue dots) at two detection wavelengths, 470 nm and 552 nm, as marked in Fig. 2a and b, showing the single-wavelength absorption transients (top panel) and residuals (bottom panel). The residuals (Δ = data – global model) are shown with a 2.5× zoom factor for the absorbance ordinate.

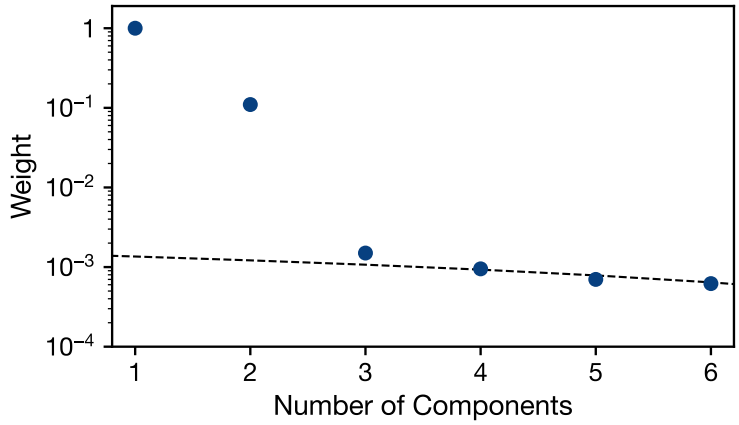

Figure S9. Singular-value decomposition analysis of the time evolution of the absorption spectrum of OCP at 293 K in the absence of glycerol in the dark following continuous 430-nm illumination (275 µW).

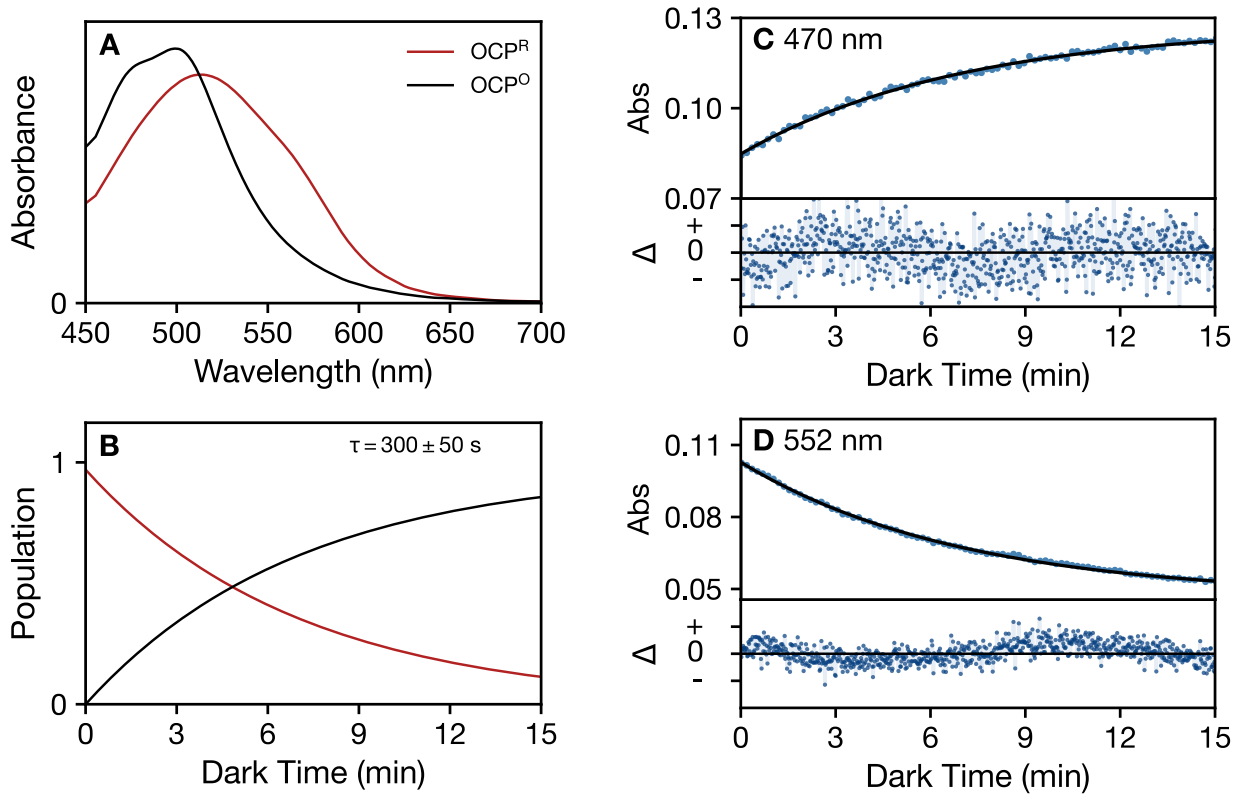

Figure S10. Global modeling of the time evolution of the absorption spectrum of OCP at 293 K in the absence of glycerol in the dark following continuous 430-nm illumination (545 µW), applying a two-compartment kinetic model: $OCP^R \xrightarrow{1/\tau} OCP^O$. (a) Evolution

associated absorption spectra for the two kinetic compartments: dark-adapted OCP^O reactant (black) and the final OCP^R product (red). (b) Time evolution of the populations for the OCP^O and OCP^R kinetic compartments; the initial mixture of $OCP^R(0) = 0.95$ and $OCP^O(0) = 0.05$ was determined from modeling of the prior photoactivation response. (c, d) Fit of the global model (black) to the observed absorption (blue dots) at two detection wavelengths, 470 nm and 552 nm, as marked in Fig. 2a and b, showing the single-wavelength absorption transients (top panel) and residuals (bottom panel). The residuals (Δ = data – global model) are shown with a 20× zoom factor for the absorbance ordinate.

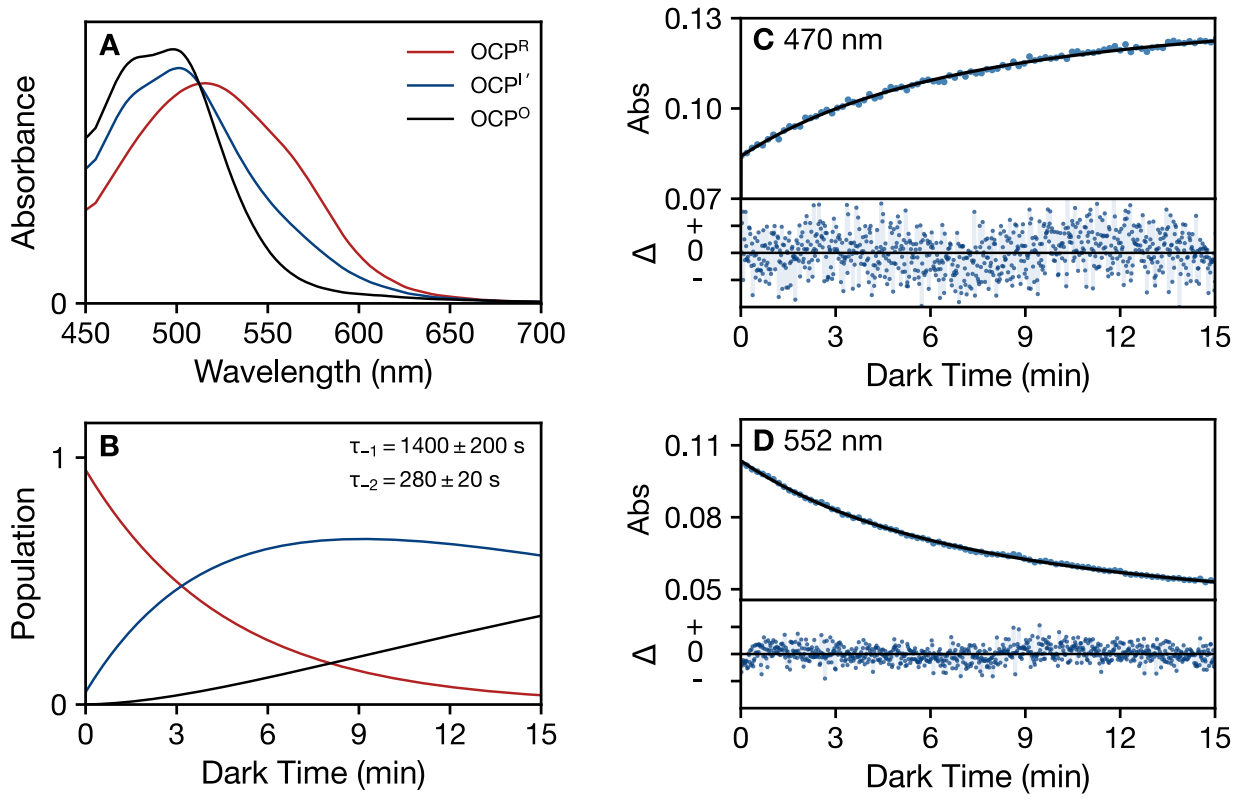

Figure S11. Global modeling of the time evolution of the absorption spectrum of OCP at 293 K in the absence of glycerol in the dark following continuous 430-nm illumination (545 μW), applying a three-compartment kinetic model: $OCP^R \xrightarrow{1/\tau_{-2}} OCP^{I'} \xrightarrow{1/\tau_{-1}} OCP^O$. (a) Evolution-associated absorption spectra for the three kinetic compartments: OCP^R reactant (red), the $OCP^{I'}$ intermediate (blue), and the final OCP^O product (black). (b) Time evolution of the populations for the OCP^R, $OCP^{I'}$, and OCP^O kinetic compartments; the initial mixture of $OCP^R(0) = 0.97$, $OCP^I(0) = 0.03$, and $OCP^O = 0.00$ was determined from modeling of the prior photoactivation response. (c, d) Fit of the global model (black) to the observed

absorption (blue dots) at two detection wavelengths, 470 nm and 552 nm, showing the single-wavelength absorption transients (top panel) and residuals (bottom panel). The residuals (Δ = data – global model fit) are shown with a 20× zoom factor for the absorbance ordinate.

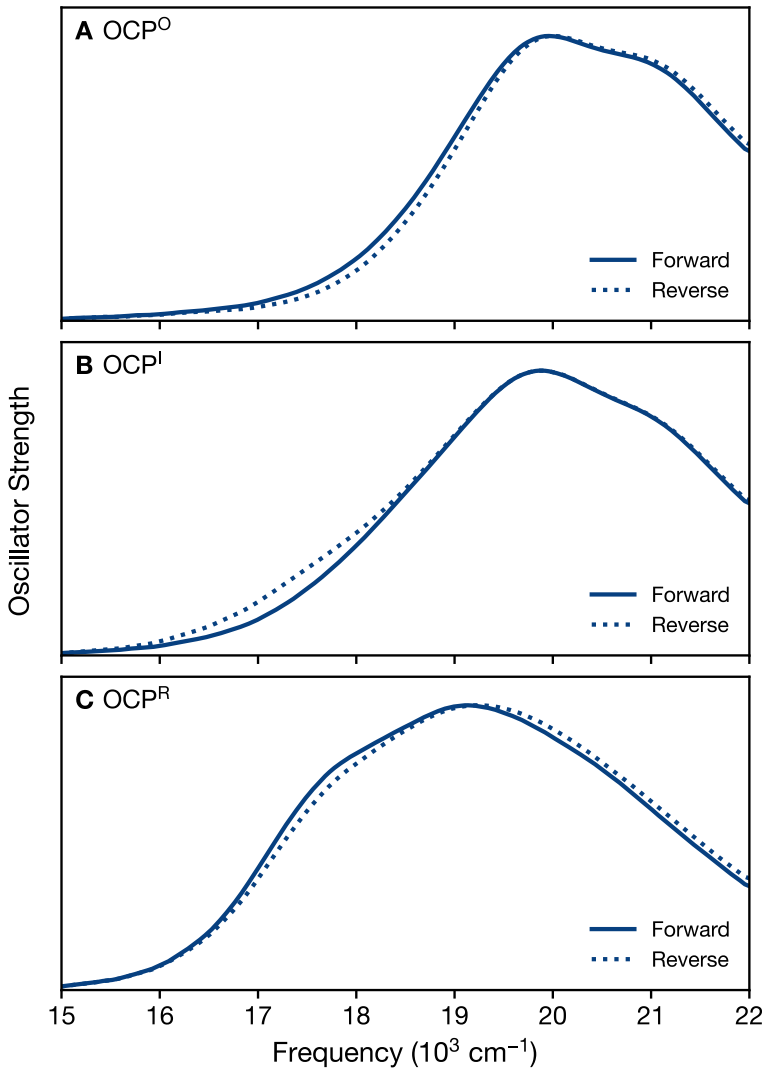

Figure S12. Comparison of the evolution-associated spectra obtained from the global models for the forward photoactivation (Fig. 6) and reverse dark recovery (Fig. S11) responses of OCP at 293 K in the absence of glycerol.

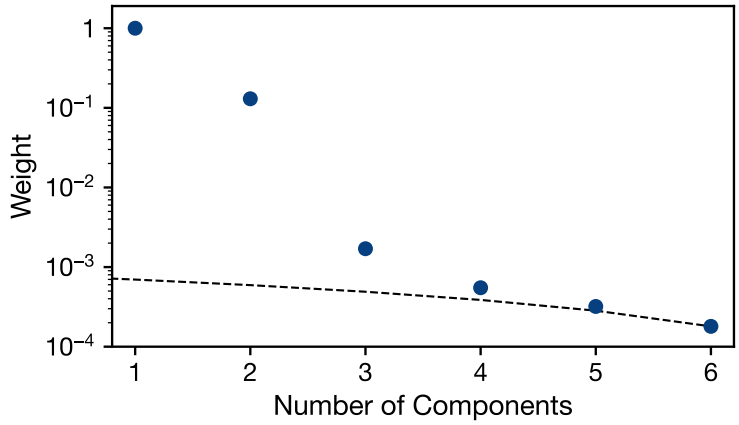

Figure S13. Singular-value decomposition analysis of the time evolution of the absorption spectrum of OCP at 293 K in the presence of 60% (v/v) glycerol during continuous 430-nm illumination (275 µW). The dashed line marks the noise level of the data set.

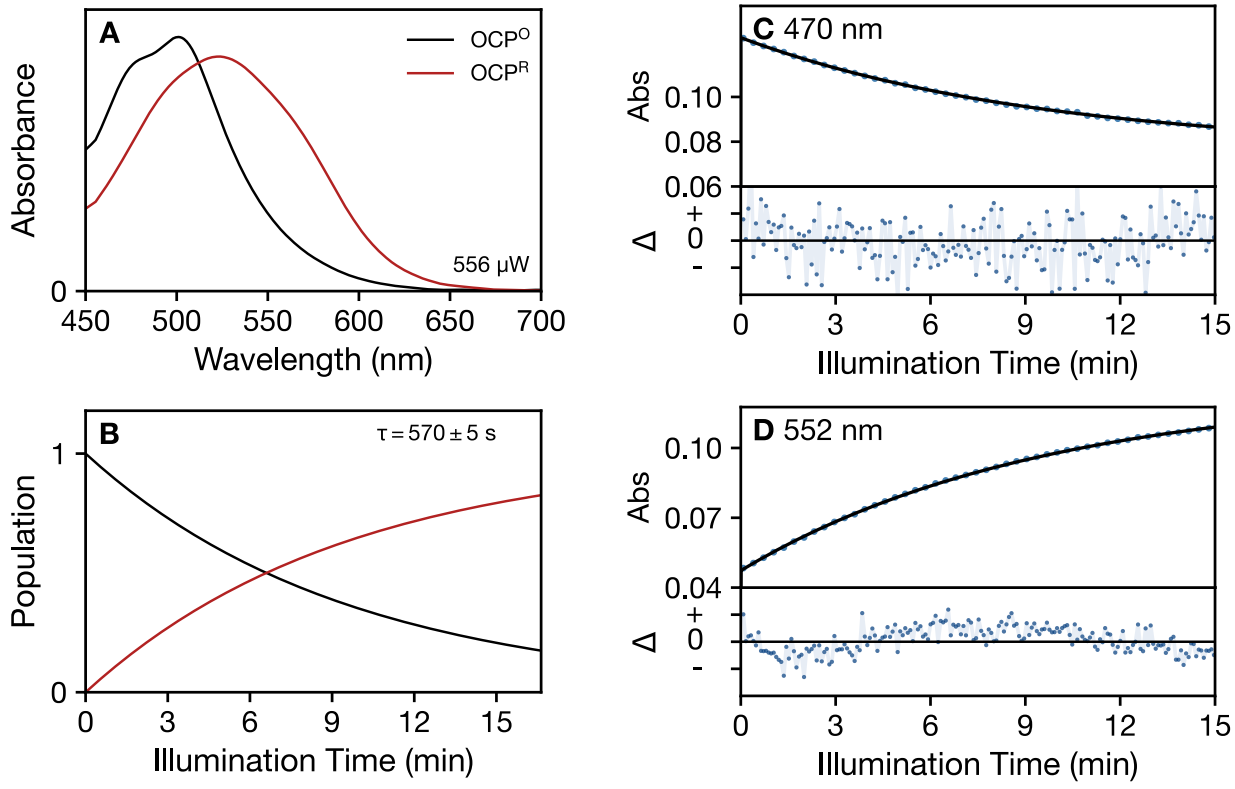

Figure S14. Global modeling of the time evolution of the absorption spectrum of OCP at 293 K in the presence of 60% (v/v) glycerol under continuous 430-nm illumination (556 µW), applying a two-compartment kinetic model: $OCP^O \xrightarrow{1/\tau} OCP^R$. (a) Evolution-

associated absorption spectra for the two kinetic compartments: dark-adapted OCP^O reactant (black) and the final OCP^R product (red). (b) Time evolution of the populations for the OCP^O and OCP^R kinetic compartments. (c, d) Fit of the global model (black) to the observed absorption (blue dots) at two detection wavelengths, 470 nm and 552 nm, as marked in Fig. 2a and b, showing the single-wavelength absorption transients (top panel) and residuals (bottom panel). The residuals (Δ = data – global model) are shown with a 20× zoom factor for the absorbance ordinate.

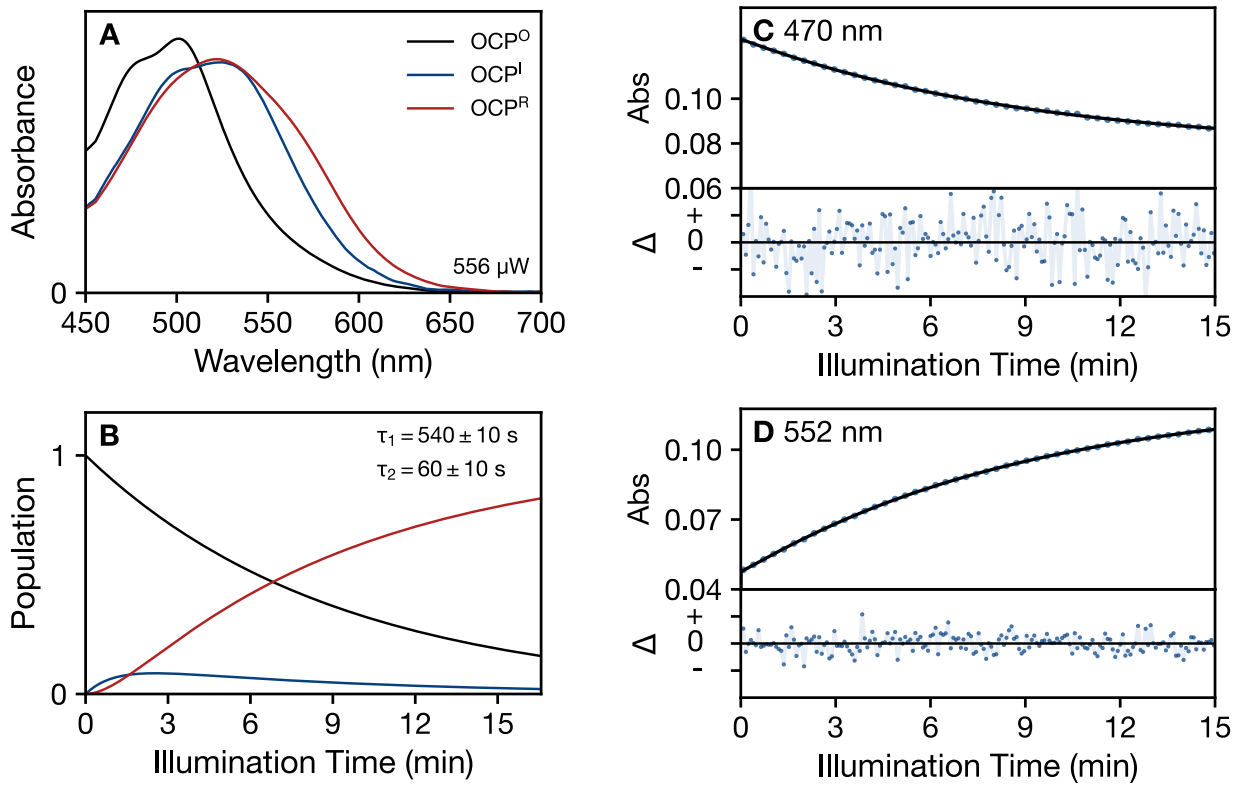

Figure S15. Global modeling of the time evolution of the absorption spectrum of OCP at 293 K in the presence of 60% (v/v) glycerol under continuous 430-nm illumination (556 µW), applying a three-compartment kinetic model: $OCP^O \xrightarrow{1/\tau_1} OCP^I \xrightarrow{1/\tau_2} OCP^R$. (a) Evolution-associated absorption spectra for the three kinetic compartments: dark-adapted OCP^O reactant (black), the OCP^I intermediate (blue), and the final OCP^R product (red). (b) Time evolution of the populations for the OCP^O, OCP^I, and OCP^R kinetic compartments. (c, d) Fit of the global model (black) to the observed absorption (blue dots) at two detection wavelengths, 470 nm and 552 nm, as marked in Fig. 2a and b, showing the single-wavelength absorption transients (top panel) and residuals (bottom panel). The

residuals (Δ = data – global model) are shown with a 20× zoom factor for the absorbance ordinate.

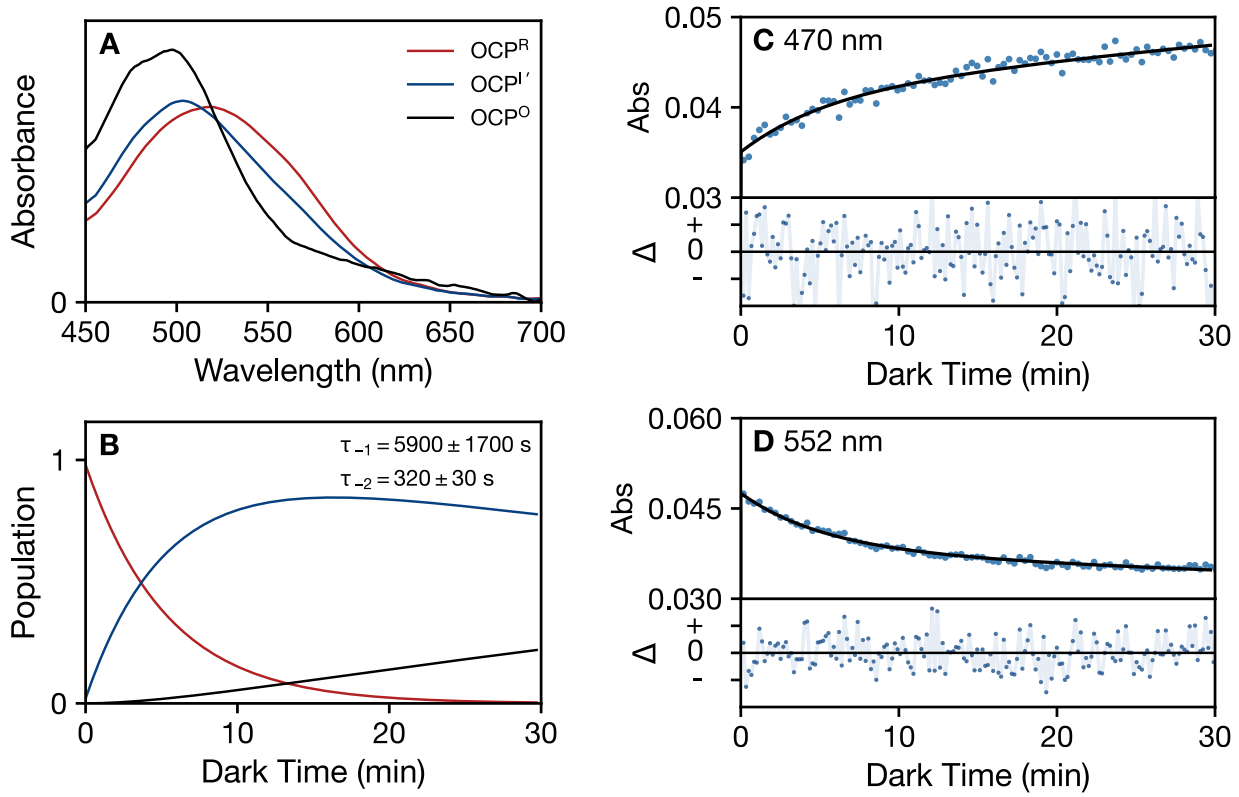

Figure S16. Global modeling of the time evolution of the absorption spectrum of OCP at 293 K in the dark in the absence of glycerol following continuous 430-nm illumination (700 µW), applying a three-compartment kinetic model: $OCP^R \xrightarrow{1/\tau_{-2}} OCP^{I'} \xrightarrow{1/\tau_{-1}} OCP^O$. The absorption at 500 nm of the dark adapted OCP^R solution present prior to illumination was 0.06. (a) Evolution-associated absorption spectra for the three kinetic compartments: OCP^R reactant (red), the $OCP^{I'}$ intermediate (blue), and the final OCP^O product (black). (b) Time evolution of the populations for the OCP^R, $OCP^{I'}$, and OCP^O kinetic compartments; the initial mixture of $OCP^R(0) = 0.98$, $OCP^{I'}(0) = 0.02$, and $OCP^O(0) = 0.00$ was determined from modeling of the prior photoactivation response. (c, d) Fit of the global model (black) to the observed absorption (blue dots) at two detection wavelengths, 470 nm and 552 nm, showing the single-wavelength absorption transients (top panel) and residuals (bottom panel). The residuals (Δ = data – global model fit) are shown with a 5× zoom factor for the absorbance ordinate.

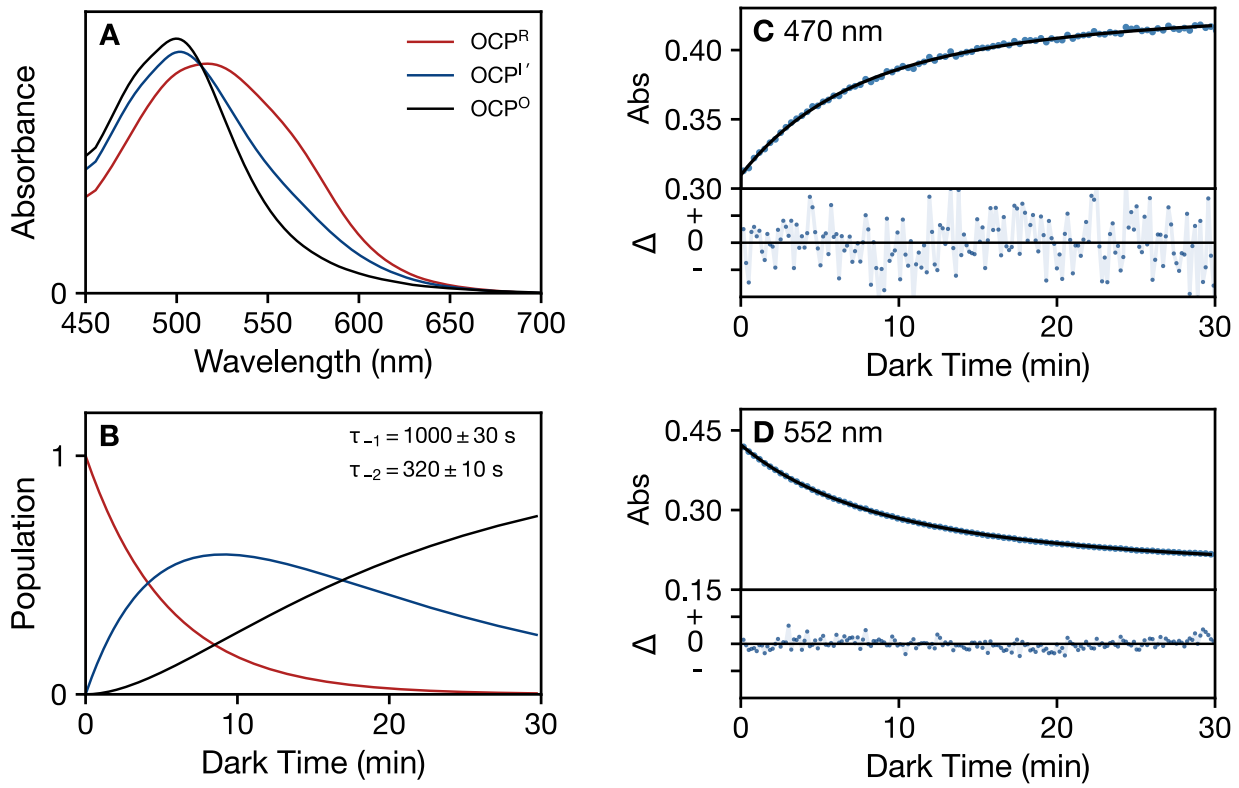

Figure S17. Global modeling of the time evolution of the absorption spectrum of OCP at 293 K in the dark in the absence of glycerol following continuous 430-nm illumination (700 μW), applying a three-compartment kinetic model: $OCP^R \xrightarrow{1/\tau_{-2}} OCP^{I'} \xrightarrow{1/\tau_{-1}} OCP^O$. The absorption at 500 nm of the dark adapted OCP^R solution present prior to illumination was 0.6. (a) Evolution-associated absorption spectra for the three kinetic compartments: OCP^R reactant (red), the $OCP^{I'}$ intermediate (blue), and the final OCP^O product (black). (b) Time evolution of the populations for the OCP^R, $OCP^{I'}$, and OCP^O kinetic compartments; the initial mixture of $OCP^R(0)$ = 1.00, $OCP^I(0)$ = 0.00, and $OCP^O(0)$= 0.00 was determined from modeling of the prior photoactivation response. (c, d) Fit of the global model (black) to the observed absorption (blue dots) at two detection wavelengths, 470 nm and 552 nm, showing the single-wavelength absorption transients (top panel) and residuals (bottom panel). The residuals (Δ = data – global model fit) are shown with a 20× zoom factor for the absorbance ordinate.

Table S1. Multimode Brownian oscillator (MBO) model parameters[a,b] for the simulated absorption spectra shown in Fig. 7 for canthaxanthin (CAN) in 2-methyltetrahydrofuran and in the photoactivation of OCP at 293 K in the absence of glycerol.

		Reorganization Energies					
Species	ω_{eg}	G	E_1	E_2	ν_1	ν_2	λ
CAN/ 2-MTHF	21330	400	600	400	810	750	2960
OCP^O	20880	350	200	500	480	730	2260
OCP^I	20550	260	320	400	1350	600	2930
OCP^R	19700	90	750	800	880	1200	3720

a. See Gurchiek et al.[1] for an explanation of the parameters and of the associated theory. As in that work, the MBO model used here incorporates an inertial solvation mode (G), two diffusive solvation modes (E_1 and E_2), and two underdamped vibrational modes of the CAN chromophore (the C–C stretching mode, $\nu_1 = 1150$ cm^{-1} and the C= C stretching mode, $\nu_2 = 1550$ cm^{-1}).

b. All parameters have units of wavenumbers (cm^{-1}). The ω_{eg} values are for the vertical $S_0 \rightarrow S_2$ energy gap for CAN's absorption transition, but the remaining parameters are for the reorganization energies λ_i for the given mode. The total of the reorganization energies is provided in the λ column.

Analysis of the Kinetics of the Dark Recovery Response

The concentration dependence of the global model rate constants (Fig. 7) determines the molecularity of the two steps in the dark recovery mechanism:

$$OCP^R \xrightarrow{k_{-2}} OCP^O \quad \text{(S1)}$$

$$2\ OCP^O \xrightarrow{k_{-1}} (OCP^O)_2 \quad \text{(S2)}$$

Conversion of OCP^R to OCP^O (eq. S1) is a unimolecular reaction, with first-order kinetics with respect to the OCP^R protein concentration. Because each of these monomeric molecular species contains a single canthaxanthin (CAN) chromophore, the kinetics are also first order with respect to the signal detected by the absorption spectrophotometer. Fig. 7 shows that the rate constant k_{-2} obtained by global modeling is accordingly independent of the OCP concentration.

The second reaction in the dark recovery mechanism (eq. S2) is a bimolecular reaction of two OCP^O monomers. By inspection of eq. S2, the rate of formation of the $(OCP^O)_2$ dimer product is second order with respect to the protein concentration of the reactant OCP^O monomer.

$$\frac{\mathrm{d}[(\mathrm{OCP^O})_2]}{\mathrm{d}t} = k_{-1}[\mathrm{OCP^O}]^2 \tag{S3}$$

But the two OCP^O monomer reactants in eq. S2 together correspond to the $OCP^{I'}$ spectroscopic intermediate:

$$\mathrm{OCP^{I'}} \equiv 2\ \mathrm{OCP^O} \tag{S4}$$

The absorption signal (S) exhibits first order kinetics for conversion of $OCP^{I'}$ to OCP^O:

$$\mathrm{OCP_S^{I'}} \xrightarrow{k_{-1,S}} \mathrm{OCP_S^O} \tag{S5}$$

$$\frac{\mathrm{d}\left[\mathrm{OCP_S^O}\right]}{\mathrm{d}t} = k_{-1,S}\left[\mathrm{OCP_S^{I'}}\right] \propto k_{-1,S} \times 2[\mathrm{OCP^O}] \tag{S6}$$

where $k_{-1,S}$ denotes the first order rate constant obtained from the global model for the absorption signal's response, and the last step in eq. S6 uses the Beer–Lambert law proportionality of the absorption signal from $OCP^{I'}$ to the protein concentration of the OCP^O monomers (eq. S4).

Given that the rate of formation of the OCP_S^O kinetic compartment corresponds to the rate of formation of the $(OCP^O)_2$ dimer complex,

$$\frac{\mathrm{d}\left[\mathrm{OCP_S^O}\right]}{\mathrm{d}t} \propto \frac{\mathrm{d}[(\mathrm{OCP^O})_2]}{\mathrm{d}t} \tag{S7}$$

we can combine eq. S6 and eq. S3 to obtain

$$2k_{-1,S}[\mathrm{OCP^O}] \propto k_{-1}[\mathrm{OCP^O}]^2 \tag{S8}$$

This result establishes that

$$k_{-1,S} \propto \frac{1}{2} k_{-1}[\mathrm{OCP^O}] \quad \text{(S9)}$$

Thus, just as observed in Fig. 7, the rate constant determined by the global model using first-order spectroscopic kinetics ($k_{-1,S}$) turns out to be linearly proportional to the concentration of the protein with a zero intercept.

Computational Methods

MD simulations were run for solvated systems on Nvidia GPU hardware with the program Desmond as implemented in the Schrödinger 2023-1 suite. The two systems were constructed using Maestro to model the OCP^O monomer and OCP^O dimer states, both containing the ketocarotenoid ligand canthaxanthin. The protein and ligand coordinates for both systems were taken from the X-ray crystal structure of OCP^O from *Synechocystis* sp. PCC 6803 (pdb ID 4xb5). The Protein Preparation application was used to preprocess the protein-ligand complex, assigning bond orders and adding hydrogens. For the alternative positions of side chains reported in the crystal structures, the most populated ones were used. Optimization of the hydrogen bond assignments was performed with default parameters (pH 7.0). The protein systems were solvated in a rectangular box with a buffer of 10 Å around the protein using the SPC water model. Protein and ligand force field parameters where defined according to OPLS4.[2] In total, the solvated system contained 34353 atoms for the monomer, and 60038 atoms for the dimer. The system was neutralized with Na^+ ions. MD calculations were carried out for 200 ns. Before performing production MD, the systems were relaxed using a multi-stage protocol that included a minimization and short MD simulations. After energy minimizations, the systems were relaxed using the following protocol:

1. Brownian dynamics simulation in the NVT ensemble at 10 K with small time steps (1 fs for bonded and near forces, 3 fs for far forces) and solute non-hydrogen atoms restrained.

2. MD simulation in the NVT ensemble using a Langevin thermostat during 12 ps, at T = 10 K, with a fast temperature relaxation constant (thermostat.tau = 0.1), velocity resampling every 1 ps, and non-hydrogen solute atoms restrained. Time steps: 1 fs (bonded and near), 3 fs (far).

3. MD simulation in the NPT ensemble using a Langevin thermostat and a Langevin barostat during 12 ps, at T = 10 K and a pressure of 1 atm, with a fast temperature relaxation constant (thermostat.tau = 0.1), a slow pressure relaxation constant (barostat.tau = 50.0), velocity resampling every 1 ps, and non-hydrogen solute atoms restrained. Time steps: 2 fs (bonded and near), 6 fs (far).

4. MD simulation in the NPT ensemble using a Langevin thermostat and a Langevin barostat during 12 ps, at T = 300 K and a pressure of 1 atm, with a fast temperature relaxation constant (thermostat.tau = 0.1), a slow pressure relaxation constant (barostat.tau = 50.0), velocity resampling every 1ps, and non-hydrogen solute atoms restrained. Time steps: 2 fs (bonded and near), 6 fs (far).

5. MD simulation in the NPT ensemble using a Langevin thermostat and a Langevin barostat during 24 ps, at T = 300 K and a pressure of 1 atm, with a fast temperature relaxation constant (thermostat.tau = 0.1) and a normal pressure relaxation constant (barostat.tau = 2.0). Time steps: 2 fs (bonded and near), 6 fs (far).

From the MD production simulations, 1000 snapshots were taken to compute averages. SASA values (in $Å^2$) were computed with respect to the ligand CAN. Histograms in Figure 7 were done using a width of 1.5 $Å^2$.

References

1 J. K. Gurchiek, H. Bao, M. A. Domínguez-Martín, S. E. McGovern, C. E. Marquardt, J. D. Roscioli, S. Ghosh, C. A. Kerfeld and W. F. Beck, Fluorescence and Excited-State Conformational Dynamics of the Orange Carotenoid Protein, *J. Phys. Chem. B*, 2018, **122**, 1792–1800.

2 C. Lu, C. Wu, D. Ghoreishi, W. Chen, L. Wang, W. Damm, G. A. Ross, M. K. Dahlgren, E. Russell, C. D. Von Bargen, R. Abel, R. A. Friesner and E. D. Harder, OPLS4: Improving Force Field Accuracy on Challenging Regimes of Chemical Space, *J. Chem. Theory Comput.*, 2021, **17**, 4291–4300.